The 3D crustal structure of the Wilkes Subglacial Basin, East Antarctica, based on joint inversion of gravity and magnetic data using variation of information.

Maximilian Lowe[1,2], Tom Jordan[1], Max Moorkamp[3], Jörg Ebbing[4], Chris Green[5], Mareen Lösing[6, 7]

Robert Larter[1]

[1] NERC British Antarctic Survey, Cambridge, United Kingdom.
[2] School of Geosciences, University of Edinburgh, Edinburgh, United Kingdom.
[3] Department of Earth and Environmental Sciences, Ludwig Maximilian University of Munich, Munich, Germany
[4] Institute of Geosciences, Kiel University, Kiel, Germany
[5] School of Earth and Environment, University of Leeds, Leeds, United Kingdom.
[6] School of Earth Sciences, University of Western Australia, Perth, Australia.
[7] Australian Centre of Excellence for Antarctic Science, University of Western Australia, Perth, Australia

Corresponding author: Maximilian Lowe (maxwe32@bas.ac.uk)

Key Points:

- Crustal density and susceptibility distribution model based on joint inversion of gravity and magnetic data using variation of information
- Crustal heterogeneities related to intrusive crustal block and the craton margin are revealed using density and susceptibility relationship
- A new tectonic evolution sketch includes two intrusion events, which are separated in time and space.

Abstract

Direct geological information in Antarctica is limited to ice free regions along the coast, high mountain ranges or isolated nunataks. Therefore, indirect methods are required to reveal subglacial geology and heterogeneities in crustal properties, which are critical steps towards interpreting geological history. We present a 3D crustal model of density and susceptibility distribution in the Wilkes Subglacial Basin and the Transantarctic Mountains (TAM) based on joint inversion of airborne gravity and magnetic data. The applied "variation of information" technique enforces a coupling between gravity and magnetic sources to give an enhanced inversion result. Our model reveals a large-scale body located in the interior of the Wilkes Subglacial Basin interpreted as a batholithic intrusive structure, as well as a linear dense body at the margin of the Terre Adélie Craton. Density and susceptibility relationships

are used to inform the interpretation of petrophysical properties and the reconstruction of the origin of those crustal blocks. The petrophysical relationship indicates that the postulated batholitic intrusion is granitic, but independent from the Granite Harbour Igneous Complex previous described in the TAM area. Emplacement of a large volume of intrusive granites can potentially elevate local geothermal heat flow significantly. Finally, we present a tectonic evolution sketch based on the inversion results, which includes development of a passive continental margin with seaward dipping basalt horizons and magmatic underplating followed by two distinct intrusion events in the Wilkes Subglacial Basin with Pan-African ages (700 - 551 Ma) and Ross ages (550 - 450 Ma).

Plain Language Summary

Most rocks in Antarctica are hidden beneath a thick icesheet. Therefore, indirect techniques are required to reveal rock provinces below the ice and within Earth's crust. Rocks simultaneously influence the gravity and magnetic field through their physical properties (density and susceptibility). Here we use both the gravity and magnetic field to reveal rock provinces beneath the ice and use the relationship between density and susceptibility of the rocks to interpret the distribution of granitic rocks in the area of the Transantarctic Mountains and the Wilkes Subglacial Basin in East Antarctica. Granitic rocks can lead to elevated heat flow due to radiogenic decay of minerals within the rock and influence the overlaying icesheet. Lastly, we use our subsurface model of rock provinces to speculate on the tectonic evolution of the region.

1 Introduction

The Wilkes Subglacial Basin (WSB) is located between the Transantarctic Mountains (TAM) and the Terre Adélie Craton (Figure 1). It was first described based on radar data in the 1970s[*Drewry*, 1976] and stretches ca 1600 km from the George V Coast towards the South Pole, while its width decreases from ca 600 km close to the George V coast [*Ferraccioli et al.*, 2009b] to < 100 km towards the South Pole [*Studinger et al.*, 2004].

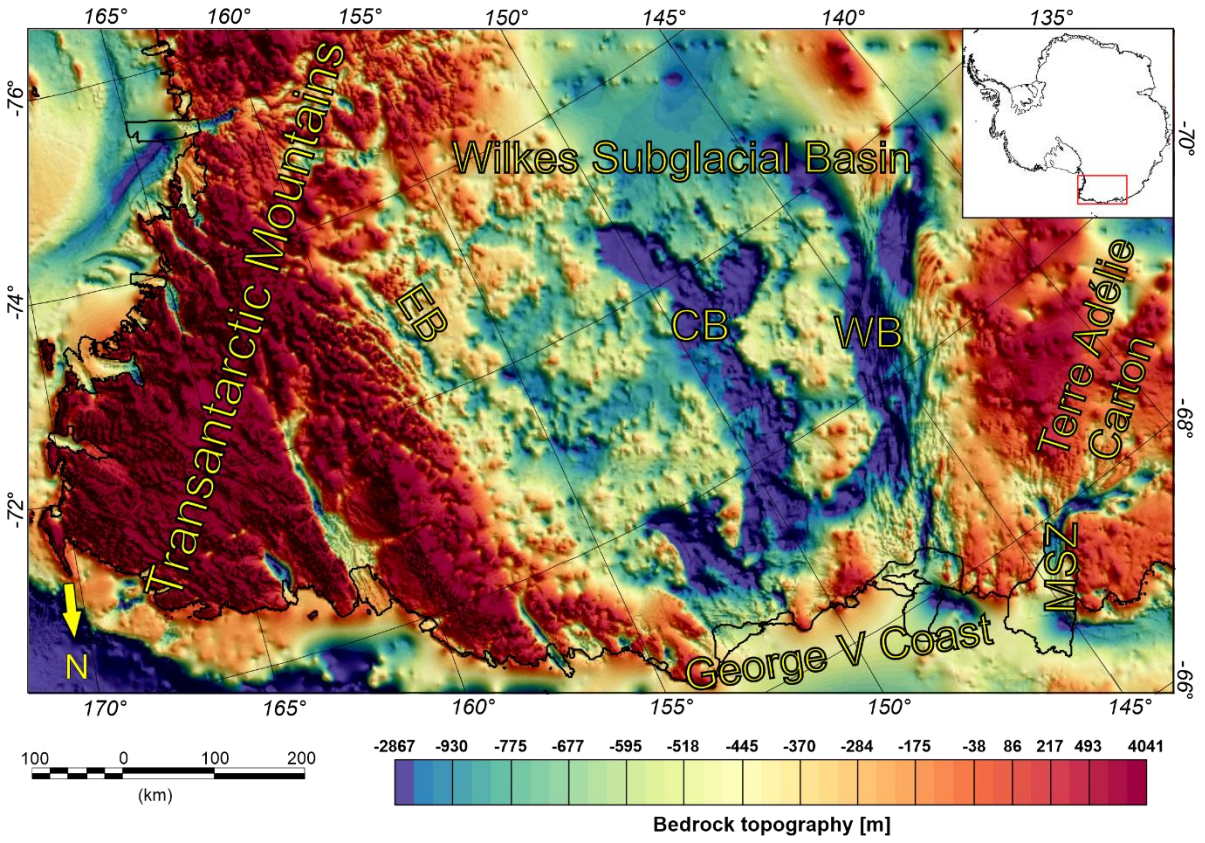

Figure 1: Bedrock topography of the Transantarctic Mountains and Wilkes Subglacial Basin (WSB) from the Bedmachine model version 2 [Morlighem et al., 2020]. EB: Eastern Basin; CB: Central Basin; WB: Western Basin; MSZ: Mertz shear zone. Black lines mark ice grounding lines and ice shelf extents from the SCAR Antarctic Digital Database.

The WSB hosts one of the largest areas of bed topography below sea level in East Antarctica, reaching depths of more than 2 km below sea level within the locally more deeply incised sub-basins [*Morlighem et al.*, 2020] (Figure 1). Such sub sea level basins pose a potentially high, but poorly understood, risk for the stability of the East Antarctic Ice Sheet (EAIS) and therefore for future sea level rise, as they are more vulnerable to melting by warming of the adjacent ocean. Such melting could potentially trigger mechanisms of unstable retreat [*Pollard et al.*, 2015; *Schoof*, 2007]. Recent

studies suggest a significant long-term contribution from the WSB region to sea-level rise within the next two centuries accompanied by major retreat of the ice sheet in the WSB region by the year 2500 [*DeConto and Pollard*, 2016; *Stokes et al.*, 2022]. For the WSB itself, competing models for its evolution have been proposed since its discovery including a rift basin[*Steed*, 1983], extended terrane [*Ferraccioli et al.*, 2001] or flexural down-warp of cratonic lithosphere as a consequence of the TAM uplift [*Stern and ten Brink*, 1989; *ten Brink et al.*, 1997]. However, the modern landscape formation of the WSB is believed to result from lithospheric flexure associated with the TAM uplift combined with glacial erosion [*Ferraccioli et al.*, 2009a; *Jordan et al.*, 2013; *Paxman et al.*, 2018; *Paxman et al.*, 2019]. The geology of the WSB remains disputed as the occurrence of direct geological samples is limited to ice free regions along the coast, or isolated nunataks, while the origin of geological material transported to the coast by glaciers is often ambiguous. Adjacent to the Mertz shear zone, on the side of the Terre Adélie Craton, ≥2440 Ma old paragneiss and granitoids are exposed, while on the WSB side of the Mertz shear zone ca. 500 Ma old granites have been mapped[*Goodge and Finn*, 2010]. Aeromagnetic measurements in the WSB have been used to infer the presence of Beacon Supergroup sedimentary strata intruded by rocks of the Ferrar Large Igneous Province [*Ferraccioli et al.*, 2009a]. Geological interpretations of the interior of the WSB are mainly derived from radar, gravity and magnetic airborne measurements (e.g.[*Jordan et al.*, 2013]). A prominent positive magnetic anomaly exists in the central WSB the origin of which is hypothesised to be either an intrusive arc associated with subduction [*Ferraccioli et al.*, 2009a], or a thinned crust as a result of rifting [*Ferraccioli and Bozzo*, 2003]. Another prominent feature is a positive linear gravity anomaly associated with the craton margin, which was interpreted as up-thrusted crustal material along the craton flank [*Studinger et al.*, 2004].

The neighbouring Transantarctic Mountains are the largest non-contractional mountain range on Earth, separating the warmer lithosphere of the Cretaceous-Tertiary West Antarctic rift system and the colder and older provinces of East Antarctica [*Morelli and Danesi*, 2004; *Robinson and Splettstoesser*, 1986; *ten Brink and Stern*, 1992]. Direct geological information is richer in the TAM

compared to WSB since more rock outcrops are present in the high mountain range. The five dominating Ross Orogen geological units in the TAM are from east to west the Robertson Bay Terrane, the Millen Schist, the Bowers Terrane, the Wilson Terrane and Granite Harbour Igneous Complex, which are all intruded by the Jurassic Ferrar sill complex and in places overlain by the associated extrusive Kirkpatrick basalts [Estrada et al., 2026 and references therein]. Zircon-age dating from sedimentary rocks shows a decrease in age from the Wilson Terrane eastwards to the Robertson Bay group from Pan-African age (551 – 700 Ma) to Ross age (450 -550 Ma) [*Estrada et al.*, 2016]. The age of the Granite Harbour Igneous Complex relates to the Ross Orogeny [*Estrada et al.*, 2016], while the source for the Pan African material remains speculativeThe subglacial geology in the WSB and TAM region is largely hidden beneath a 2-3 km thick ice sheet. Understanding the subglacial geology and crustal properties is crucial to constrain the influence of the solid Earth on the stability of the overlying ice sheet. Radiogenic heat production is predicted to contribute up to 40% to the surface geothermal heat flow [*Artemieva and Mooney*, 2001; *Haeger et al.*, 2022; *Hasterok and Chapman*, 2011]. However, due to the lack of information on subglacial geology and crustal properties, incorporating accurate thermal crustal parameters such as radiogenic heat production and thermal conductivity is challenging and therefore current geophysical derived geothermal heat flow models commonly use global average values instead [*Haeger et al.*, 2022; *Lösing and Ebbing*, 2021; *Lowe et al.*, 2023; *Martos et al.*, 2017; *Shen et al.*, 2020; *Stål et al.*, 2021]. For more in depth discussion of current Antarctic geothermal heat flow models the reader is referred to[*Reading et al.*, 2022] and [*Burton-Johnson et al.*, 2020].

The objectives of this study are to identify crustal structures, crustal geological provinces and intrusive bodies and constrain their dimension in 3D, and also to identify the Terre Adélie Craton boundary. For this purpose, we conduct joint inversion of gravity and magnetic data to obtain petrological parameter distribution in terms of density and susceptibility. The geophysical inversion uses the joint inversion framework JIF3D [*Moorkamp et al.*, 2011], which uses the Variation of Information (VI) to introduce a coupling between the inverted density and susceptibility sources [*Lösing et al.*, 2023; *Moorkamp*, 2021; 2022]. Subsequently, the density and susceptibility relationship of the inversion model is used

to identify crustal rock provinces and infer potential rock types. The geophysical and petrophysical interpretation of the inversion results is the basis for our tectonic evolution model.

2 Method

2.1 Joint inversion of gravity and magnetic data

Joint inversion of gravity and magnetic data is carried out in JIF3D [*Moorkamp et al.*, 2011]. JIF3D is a 3D joint inversion framework for geophysical data sets including magnetotelluric, seismic, magnetic data as well as scalar and tensor gravity data. JIF3D utilizes a limited memory quasi-Newton approach [*Avdeev and Avdeeva*, 2009] for optimization. For a complete mathematical description of the JIF3D inversion framework the reader is referred to [*Moorkamp*, 2021; 2022; *Moorkamp et al.*, 2011].

Inverting simultaneously for crustal density and susceptibility distribution using gravity and magnetic data in a joint inversion framework is well established [*Bosch et al.*, 2006; *Fregoso and Gallardo*, 2009; *Frey and Ebbing*, 2020; *Gallardo-Delgado et al.*, 2003; *Guillen and Menichetti*, 1984; *Shamsipour et al.*, 2012]. However, joint inversion based on Variation of Information (VI), which allows the coupling of physical parameters, has only recently became popular in geophysical joint inversion applications [*Haber and Holtzman Gazit*, 2013; *Lösing et al.*, 2023; *Mandolesi and Jones*, 2014; *Moorkamp*, 2021; 2022]. VI is related to the concept of mutual information (MI) [*Moorkamp et al.*, 2011]. VI describes the amount of shared information contained in two variables, meaning a low VI value indicates that both variables are dependent, while a high VI value indicates that information about variable 1 does not reveal meaningful information about variable 2 [*Lösing et al.*, 2023; *Mandolesi and Jones*, 2014; *Moorkamp*, 2021; 2022]. Variation of Information is defined as:

$$VI(x,y) = 2H(x,y) - H(x) - H(y) \quad (1)$$

Here $H(\mathrm{x}) = -\sum_i p(\mathrm{x_i}) \log p(\mathrm{x_i})$ is the Shannon Entropy; $p(\mathrm{x_i})$ is the probability density approximated by kernel methods [*Mandolesi and Jones*, 2014]; $H(\mathrm{x})$ and $H(y)$ are the marginal

148 entropies and $H(\mathrm{x},\mathrm{y})$ is the joint entropy[*Lösing et al.*, 2023; *Moorkamp*, 2021; 2022]. VI is
149 incorporated into the objective function Φ_{joint} as:

150 $$\Phi_{joint} = \Phi_{d,grav} + \Phi_{d,mag} + \lambda_1\Phi_{reg,\rho} + \lambda_2\Phi_{reg,sus} + \lambda_3\Phi_{VI} (2)$$

151 where $\Phi_{d,grav}$ and $\Phi_{d,mag}$ are the Root-Mean-Square (RMS) misfit between observed and inverted
152 gravity and magnetic data; $\Phi_{reg,\rho}$ and $\Phi_{reg,sus}$ are regularisation terms for the density and
153 susceptibility distribution, controlling the smoothness of the inverted model, Φ_{VI} is a coupling term
154 which includes Variation of Information of recovered density and susceptibility and λ represents

155 the weighting factors of the individual terms.

156 VI inversion has been successfully applied to magnetotelluric and seismic data [*Mandolesi and Jones*,
157 2014], magnetotelluric and gravity data [*Moorkamp*, 2021; 2022], and gravity and magnetic data
158 [*Lösing et al.*, 2023]. [*Lösing et al.*, 2023] demonstrated that VI inversion can recover density and
159 susceptibility distribution, if it is assumed that the gravity and magnetic signals have an identical
160 source, by performing VI inversion tests on synthetic data.

161 **2.1.1 Inversion setup**

162 The density and susceptibility inversion models are discretised into meshes with equal horizontal cell
163 sizes of 7.5 km. The vertical cell size is 1 km at the surface and increases with depth by a factor 1.1 for
164 each cell. Increasing vertical cell size with depth is introduced to account for decreasing resolution
165 with increasing distance to the source in potential field applications. A horizontal cell size of 7.5 km is
166 chosen because the input gravity and magnetic data have a resolution of 10 km (see section 3). A cell
167 size of 7.5 km allows the inversion to adjust on average more than one cell to fit the inversion data
168 but is also not so small that it does not represent the resolution of the input data or introduce artifacts.
169 Additionally, a padding area of 20% around the study area is added to avoid edge effects. The resulting
170 inversion mesh contains 244 cells east-west direction, 140 cells in north-south direction and 21 cells
171 in the z direction (60 km below sea level). To constrain the model geometry, the bedrock topography

from BedMachine version 3 [*Morlighem et al.*, 2020], Curie point depths (CPD) [*Lowe et al.*, 2023], and Moho depths [*Pappa et al.*, 2019a] are used.

The aim of the VI inversion is to invert jointly the gravity and magnetic field for the density and susceptibility of the crust. Only cells between the bedrock interface and the Moho interface are allowed to vary during the inversion. However, rocks lose their magnetic properties at the Curie temperature. Therefore, the Curie Depth Points from [*Lowe et al.*, 2023] are introduced as an additional constraint. Joint VI inversion is carried out for all cells between the bedrock interface and the CPD interface. Between the CPD interface and the Moho interface only density inversion is carried out and no susceptibility values are obtained for this section of the crust. The input gravity field for the density inversion is corrected for masses below the Moho interface by the Antarctic lithospheric model from Pappa et al., (2019b) (see section 3.1). All cells are set to a starting value of 0 kg/m^3 for the density anomaly model and 0 SI for the magnetic model and are iteratively updated during the VI inversion process. The first inversion run is performed with a high coupling weight in order to enforce a tight coupling between the inverted models. Subsequently, a second inversion run is carried out, which uses the resulting density and susceptibility values from the first inversion run as a starting model but a lower coupling weight is applied. The rationale behind using two different coupling weights is that a tighter coupling in the first inversion run favours geometrical structures in both the density and susceptibility, while a second inversion run with a lower coupling provides the inversion algorithm with more freedom to fit the observed gravity and magnetic field better [*Moorkamp*, 2022]. Coupling values were established by trial and error. The induced magnetic field strength is set to 64981 nT with an inclination of -84.4° and a declination of 147.4° based on the definitive magnetic reference field (DGRF) for a longitude of 155° and a latitude of -73° for the year 2005 (the year of the aerogeophysical survey WISE-ISODYN, which is the main survey in the study area). Additional parameter settings of the inversion are given in table 1.

Table 1 Inversion parameters

Coupling	25,000 run 1 and 15,000 run 2

Regularization Density and Susceptibility	10
Error Gravity [mGal]	2 mGal
Error Magnetics [nT]	15
Min. / Max Density [kg m^{-3}]	± 250
Min. / Max Susceptibility [SI]	± 0.1
Magnetic Field strength [nT]	64981
Inclination [°]	-84.4
Declination [°]	147.4
dens_covmod (Maximum depth of density variation).	Moho depth
sus_covmod (Maximum depth of susceptibility variation).	CPD depth
coupling_validity (Maximum depth where coupling is assumed).	CPD depth

Subsequently the relationship between the inverted relative densities and susceptibilities are used to characterize 3D crustal structures and to identify crustal units with similar relationships.

3 Data

This section describes the geophysical data and the boundary condition used during the VI inversion to obtain a 3D crustal density and susceptibility distribution model.

3.1 Gravity data

Bouguer gravity anomaly data are taken from AntGG [*Scheinert et al.*, 2016]. The AntGG gravity compilation includes airborne, terrestrial, and shipborne measurements, which are provided as a grid with a grid spacing of 10 km. Data gaps in AntGG are filled in with Bouguer anomaly data from the Ganovex VII – ItaliAntartide XV survey [*Reitmayr et al.*, 2003] and recent ground station measurements conducted within the Italian National Program for Antarctic Research activities [*Zanutta et al.*, 2018] (Figure S1). This data compilation is gridded with a grid spacing of 10 km and a blanking distance of 40 km using the minimum curvature gridding function in Oasis Montaj to produce the Bouguer anomaly grid of the WSB and TAM region. The Bouguer anomaly grid is subsequently upward continued to a constant observation height of 10 km (Figure 2a) using the Compudrape algorithm in Oasis Montaj. The Bouguer anomaly map shows a large negative signal in the TAM region, where a crustal root is present beneath the mountain range. A prominent positive linear feature exists in the Bouguer

anomaly map following the western edge of the Wilkes Subglacial Basin and might indicate the transition zone at the margin of the Terre Adélie Craton [*Goodge and Finn*, 2010]. To remove the gravity contribution below the Moho interface the gz gravity component from the Antarctic continent-wide forward lithospheric model from Papa et al. (2019b) was subtracted (Figure S2). This model contains a homogeneous crust and a variable mantle. By subtracting this model, we corrected for a variable mantle and Moho depth variation and therefore the resulting residuals belong to the crust. The lithospheric model is presented at 10 km observation height and is the reason all input data are upward continued to this constant height. In the resulting residual gravity map (Figure S2) the large-scale negative signal beneath the TAM is absent, while the relative positive linear crustal structure is preserved. Furthermore, the mean value (92.5 mGal) of the residual gravity field is removed to shift the residual gravity field to a mean level of 0 mGal (Figure 2b).

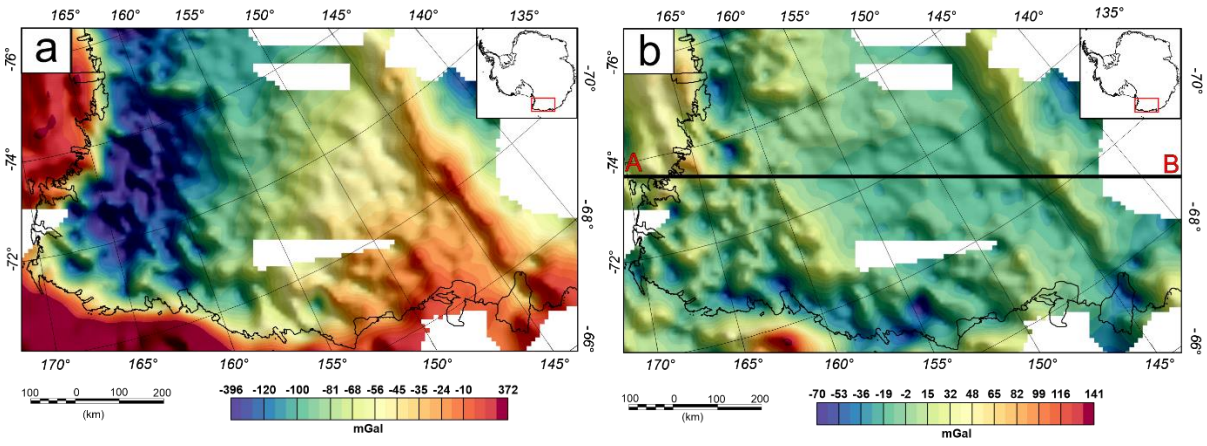

Figure 2 a) Bouguer Anomaly compilation including AntGG data [Scheinert et al., 2016] and regional gravity data [Reitmayr et al., 2003; Zanutta et al., 2018]. b) Residual gravity map obtained by subtracting gz gravity component from the lithospheric model of [*Pappa et al.*, 2019b] and then subtracting the mean value of the residual field. Both gravity grids have a grid spacing of 10 km. Black line indicates location of cross section profile in Figure 8.

3.2 Magnetic data

The ADMAP-2 compilation includes 3.5 million line-km of aeromagnetic and marine magnetic data in Antarctica and the Southern Ocean south of 60 °S [*Golynsky et al.*, 2018]. The gridded ADMAP-2 product (Figure 3a) has a grid spacing of 1.5 km and its production included subtraction of the International Geomagnetic Reference Field, diurnal effects correction, high-frequency error correction, levelling, regional gridding, and merging of regional grids into a continent-wide

compilation [*Golynsky et al.*, 2018]. For the inversion, the magnetic data from the ADMAP-2 compilation is regridded with a grid spacing of 10 km to match the resolution of the gravity data (section 3.1). Subsequently the magnetic data are also continued upward to a height of 10 km (Figure 3b) to be consistent with the gravity data. The upward continuation of the magnetic data functions as a lowpass filter, removing high frequency content, while broad magnetic anomalies are preserved. The magnetic anomaly grid shows a broad linear feature orientated southeast – northwest (F1) in the central part of the WSB the origin of which has been hypothesised to be a failed rift or an arc-related intrusive body [*Ferraccioli and Bozzo*, 2003; *Ferraccioli et al.*, 2009b]. Perpendicular to this features a positive magnetic anomaly is visible (F2). A strong linear anomaly exists west to the WSB towards the craton margin (F3), where the magnetic anomaly rapidly increases to values of ~1500 nT compared to the dominating ± 300 nT range in the WSB and TAM area. Smaller magnetic anomalies are observed offshore to the east (F4) and along the Rennick Graben and Matusevich glacier region (F5).

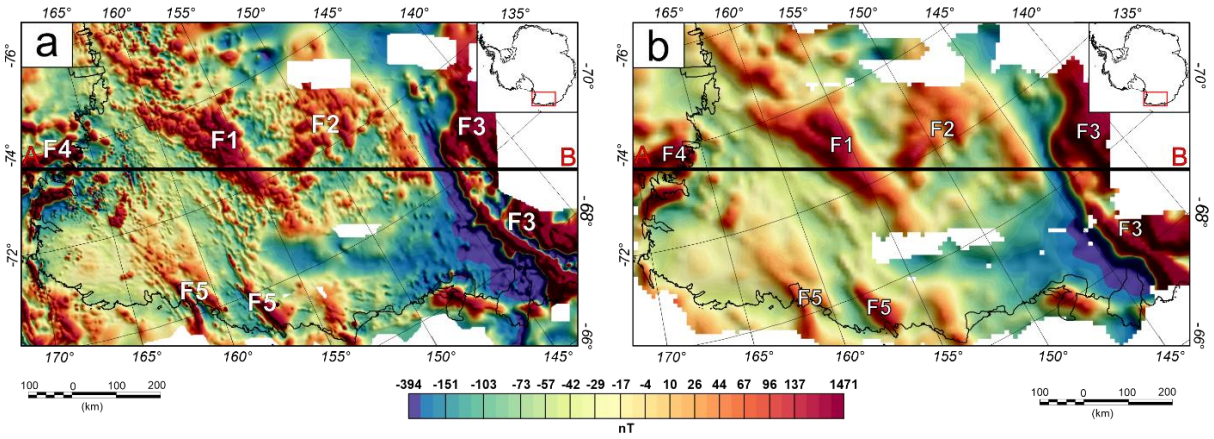

Figure 3 a) Magnetic anomaly grid from ADMAP-2 [Golynsky et al., 2018] with a grid spacing of 1.5 km. b) Regridded ADMAP-2 magnetic data with a grid spacing of 10 km and upward continued at a constant height of 10 km to match the resolution and upward-continued height of the gravity compilation. Black line indicates location of cross section profile in Figure 8. Features F1-F5 relate to magnetic anomalies discussed in the main text.

3.3 Moho depth and Curie depth.

Moho depth estimates (Figure 4a) are taken from satellite gravity inversion [*Pappa et al.*, 2019a]. The Moho interface is used as the bottom boundary condition for the density inversion.

CPD estimates are taken from [*Lowe et al.*, 2023] and used as a bottom boundary condition for the susceptibility inversion. Below the CPD the crustal rocks have lost their magnetic properties and

259 therefore the joint inversion of magnetic and gravity data needs to be limited to crustal depth above
260 the CPD. The CPD estimates from [*Lowe et al.*, 2023] have a 20 km resolution and are interpolated on
261 a 7.5 km grid, matching the cell size of the inversion mesh, by applying statistical kriging using the
262 python package PyKrig [*Murphy et al.*, 2022]. After interpolation, the CPD map shows some values
263 deeper than the Moho depths from Pappa et al. (2019a) in the offshore area and along the coast. A
264 CPD below the Moho would indicate that the upper mantle is magnetic and although this possibility
265 has been suggested [*Ferré et al.*, 2014]), we discard CPD values below the Moho boundary (Figure 4b).

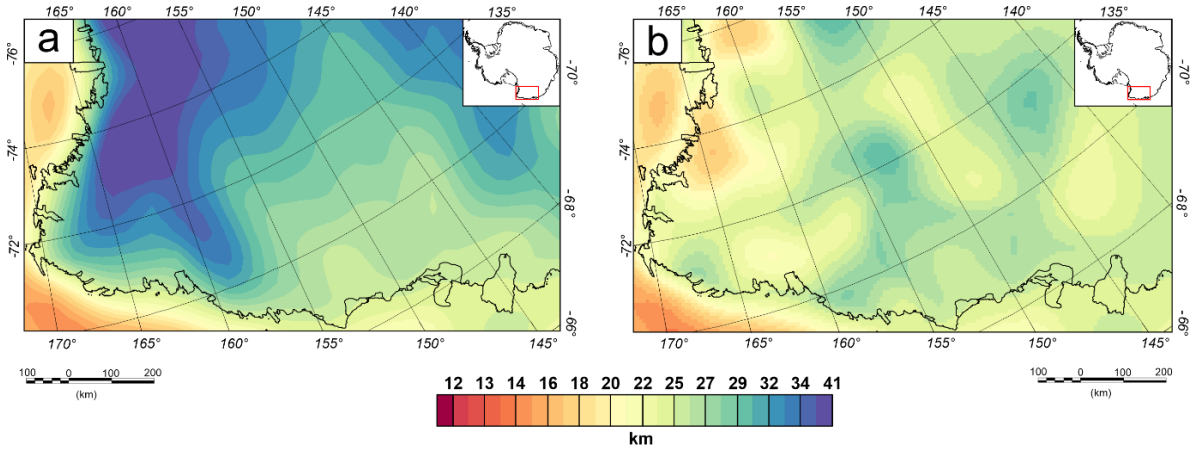

266

267 Figure 4: a) Moho depth map derived from Satellite gravity measurements [Pappa et al., 2019a]. b) Curie point depths
268 estimated [Lowe et al., 2023] based on kriging interpolation, clipped to be shallower than the Moho.

269 **4 Results**

270 The VI inversion of gravity and magnetic data for the WSB and TAM region is carried out in two
271 subsequent inversion runs with varying coupling factors of 25 000 for the first 100 iterations (inversion
272 result shown in the supporting information file) and 15 000 for subsequent 25 iterations, while all
273 other parameters are kept fixed as described in section 2.1.1 and table 1. The Root Mean Square error
274 (RMSE) after the combined 125 iterations is 1.5 mGal for the gravity inversion and 0.7 nT for the
275 magnetic inversions (Figure 5 a). The RMSE error decreases for the gravity and magnetic inversion
276 sharply after the transition from a coupling of 25 000 to 15 000 but the amplitude of decreasing RMS
277 seems not significant at first glance. However, the long wavelength residual in the magnetic inversion
278 model decreases significantly in the residual maps after lowering the coupling (Figure 6f & Figure S4)

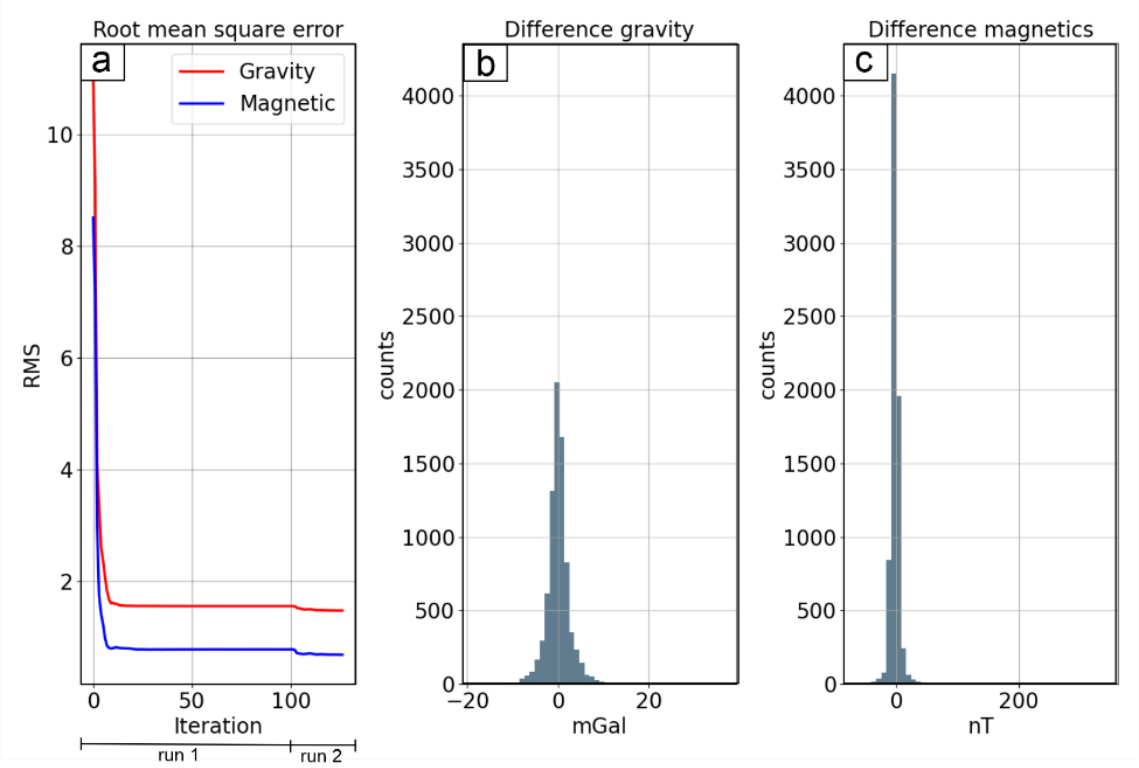

Figure 5 a) Root mean square (RMS) error between observed and inverted gravity (red) and magnetic (blue) field for each inversion iteration. b) Gravity residual histogram between observed and inverted gravity field. c) Magnetic residual between observed and inverted magnetic field.

The amplitude and distribution of anomalies within the gravity and magnetic field are reproduced well by the inversion (Figure 6a-c). The end members of the residual between observed and inverted values are + 37 and -18 mGal with a standard deviation of 3 mGal for the gravity inversion and for the magnetic inversion +341 and -65 nT with a standard deviation of 13 nT (Figure 5 c, d). The difference map between observed and inverted values are shown in figure (6 e, f). Both residual maps show a good agreement between observed and inverted gravity and magnetic field with low residuals for most of the study area. The highest misfit amplitude in the gravity field is located in the area of the TAM, in the northeastern part of the study area. Airborne surveys are sparse in this area and the AntGG [*Scheinert et al.*, 2016] compilation has significant data gaps in this region. Gravity ground stations [*Reitmayr et al.*, 2003; *Zanutta et al.*, 2018] are used to fill the data gaps (Figure S1b). A possible source of the higher amplitude in the misfit cluster in the TAM region could be contributed by the low spatial coverage of the ground stations and the offset in frequency content between the airborne and ground station data and could therefore be associated with local effects.

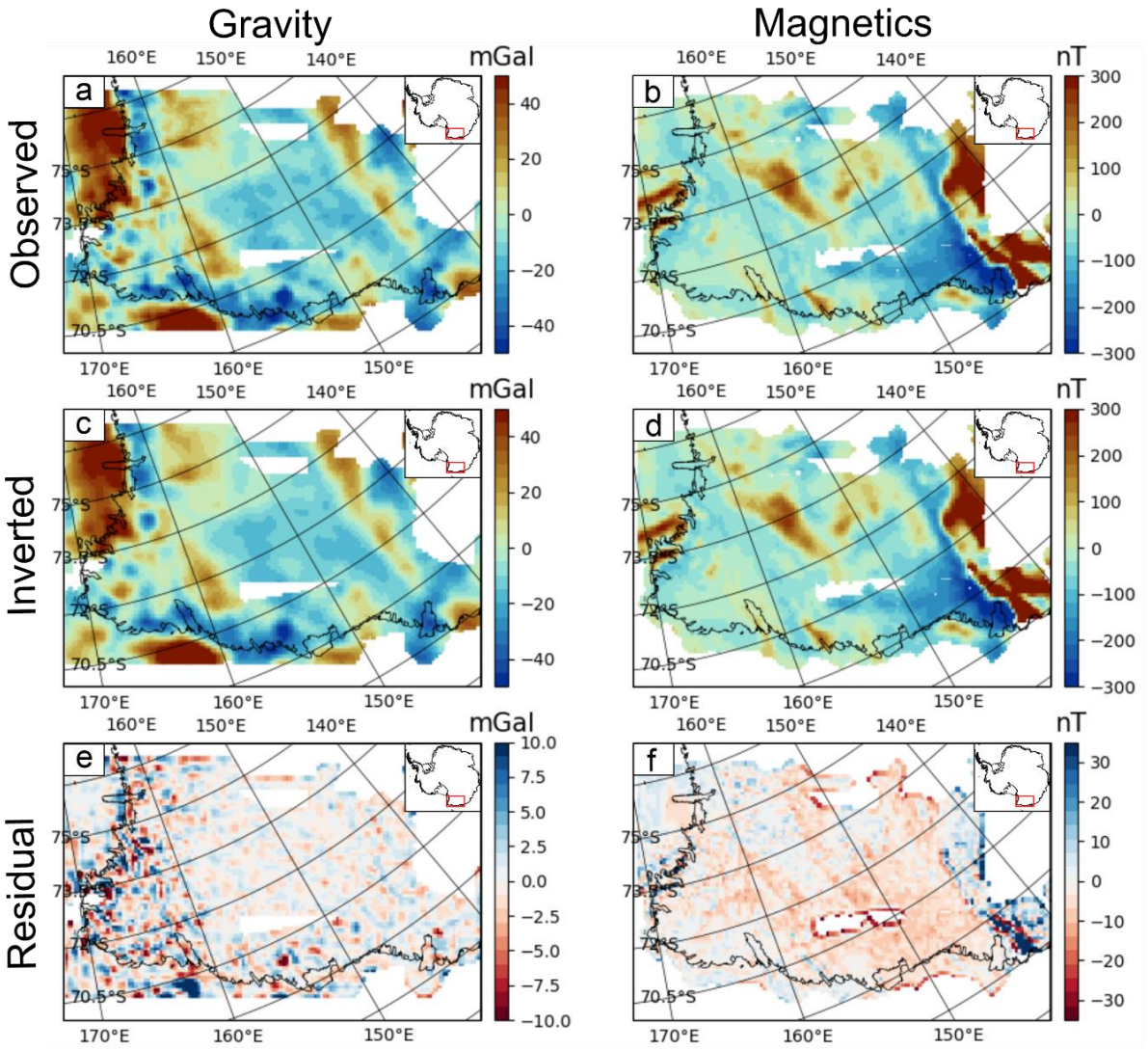

Figure 6: a) Gravity inversion input data. b) Magnetic inversion input data. c) Final inverted gravity field. d) Final inverted magnetic field. e) Difference map between observed and inverted gravity fields (6a minus 6c). f) Difference map between observed and inverted magnetic field (6b minus 6d).

The largest misfits between the observed and inverted magnetic data are located around prominent data gaps within the WSB and the large data gap in the south, as well as in the west of the study area where the amplitude of the magnetic anomaly map increases sharply from 300 nT to over 1500 nT. It is somewhat expected that the inversion algorithm struggles to reproduce a rapid variation in the magnetic field of over 1200 nT since inversion algorithms favour smooth models. On the other hand, an error of 200 nT in a region with a field strength of over 1500 nT is less dramatic than compared to the TAM and WSB region with amplitudes of 300 nT. Additionally, a long wavelength feature exists in the magnetic residual map, which we don't further address due to the low magnitude of below 5 nT.

Density and susceptibility examples at 5.5 km, 11.9 km and 20.5 km depths are presented in Figure (7). The linear southeast-northwest anomaly in the central WSB appears to be connected at depth with the neighbouring anomaly with a southeast northwest orientation, while both anomalies are separated at shallower depths.

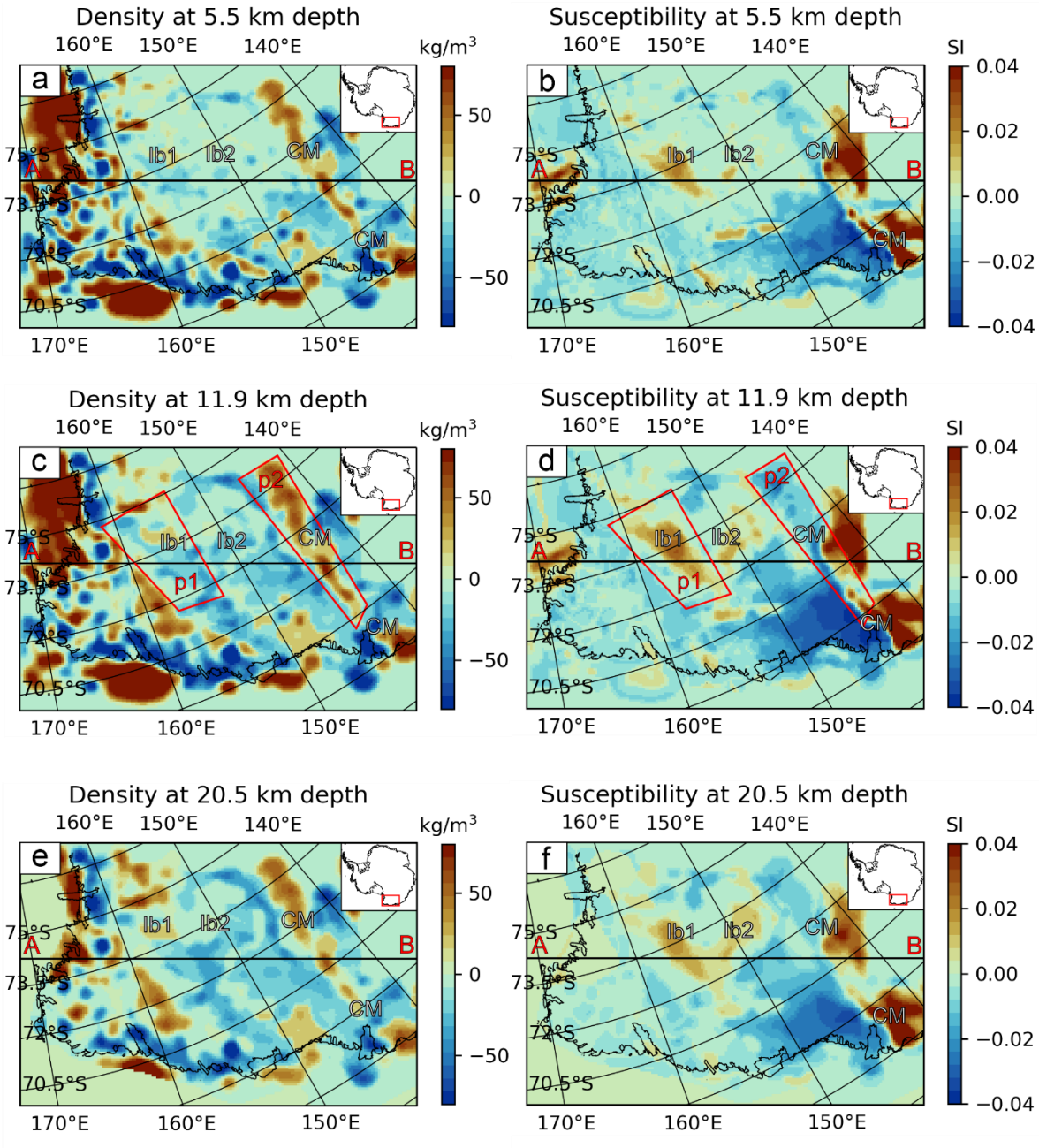

Figure 7: a) Inverted density at 5.5km depth. b) inverted susceptibility at 5.5 km depth. c) inverted density at 11.9km depth. d) inverted susceptibility at 11.9 km depth. e) inverted density at 20.5 km depth. f) inverted susceptibility at 20.5 km depth. Black line indicates location of cross section profile in Figure 8. P1 and P2 indicate the polygons for extracting 3D distribution of density and susceptibility bodies. IB: intrusive body; CM: craton margin.

317 The aim of the inversion is to find density and susceptibility distributions that are geometrically
318 connected and simultaneously can explain the observed gravity and magnetic field. The underlying
319 assumption is that a crustal rock has density and susceptibility values, which influence simultaneously
320 the gravity and magnetic field. A cross section along profile AB (Figure 2b; Figure 3a, b; Figure 8 a-f)
321 shows the similarities in the geometry of both petrophysical quantities. A large-scale negative density
322 anomaly is located centrally in profile AB (black dotted circle), while the susceptibility inversion model
323 shows a high susceptibility anomaly with identical geometry. Adjacent to this anomaly is another
324 negative density anomaly (red dotted circle) but in this case the susceptibility values are also negative.
325 This illustrates that a common geometry of both quantities is inverted, but the relationship between
326 the density and susceptibility values is not linear. The cross section through the inverted density and
327 susceptibility model indicates that the source for the linear magnetic anomaly in the central WSB is
328 connected at depth to the neighbouring anomaly source with a perpendicular orientation (Figure 8).
329 These results illustrate the advantage of using a joint inversion approach to obtain the density and
330 susceptibility distribution (see supporting information Figure S6-9).

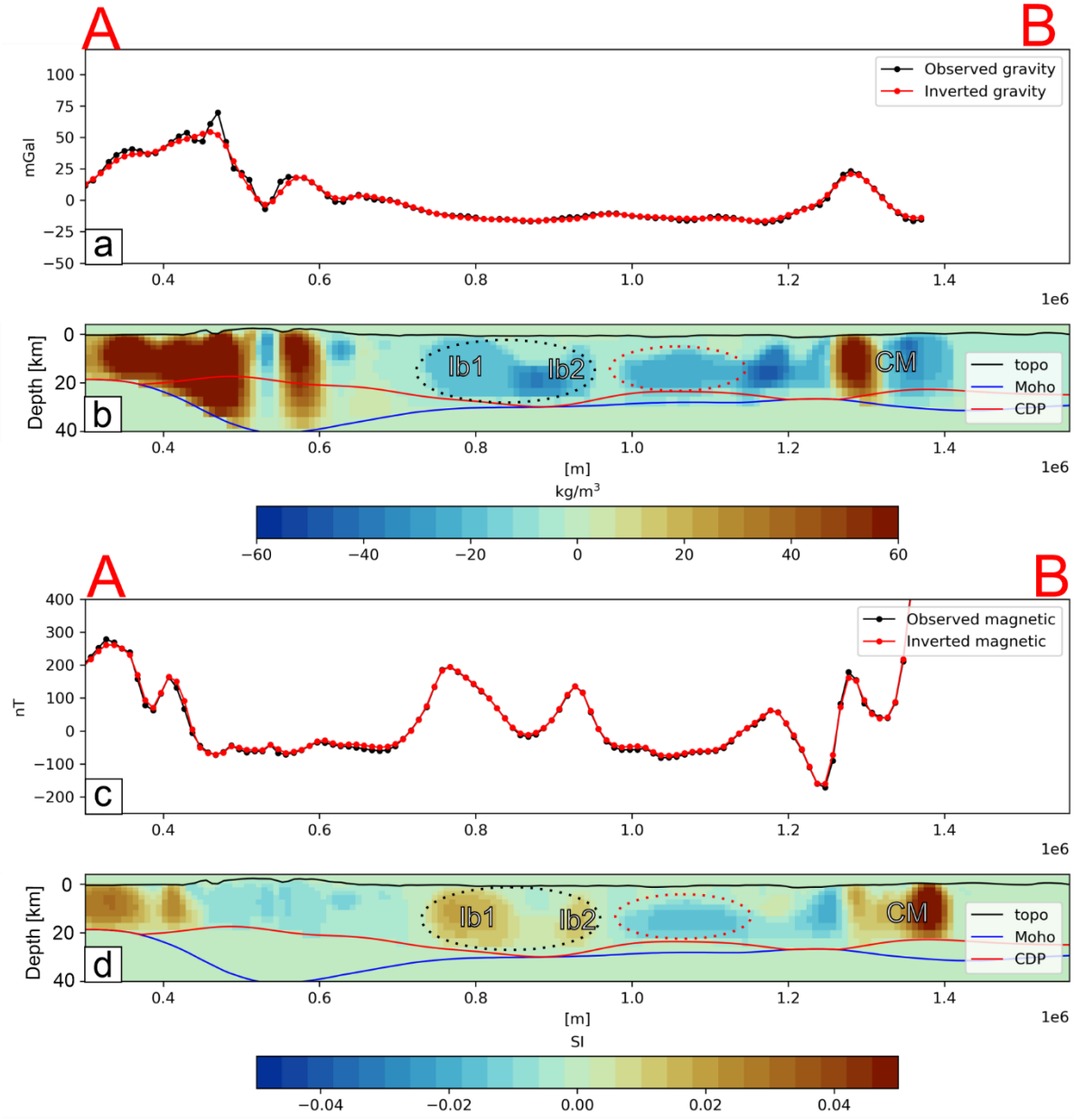

Figure 8: Observed (black line) and inverted (red line) gravity field along profile AB. Location of profile AB is given in (Figure 7). Cross-section of the inverted density model along profile AB. c) observed (black line) and inverted (red line) magnetic field along profile AB. d) cross-section of the inverted susceptibility model along profile AB. IB: intrusive body; CM: craton margin.

A density and susceptibility cross plot illustrate the parameter relationship between both quantities (Figure 9). The relative inverted densities range from -160 to 250 kg/m^3, while the inverted susceptibilities range from -0.06 to 0.9 SI. However, the density and susceptibility histograms indicate that the inverted density values are predominantly between ± 50 kg/m^3 and between ± 0.02 SI for the inverted susceptibility model.

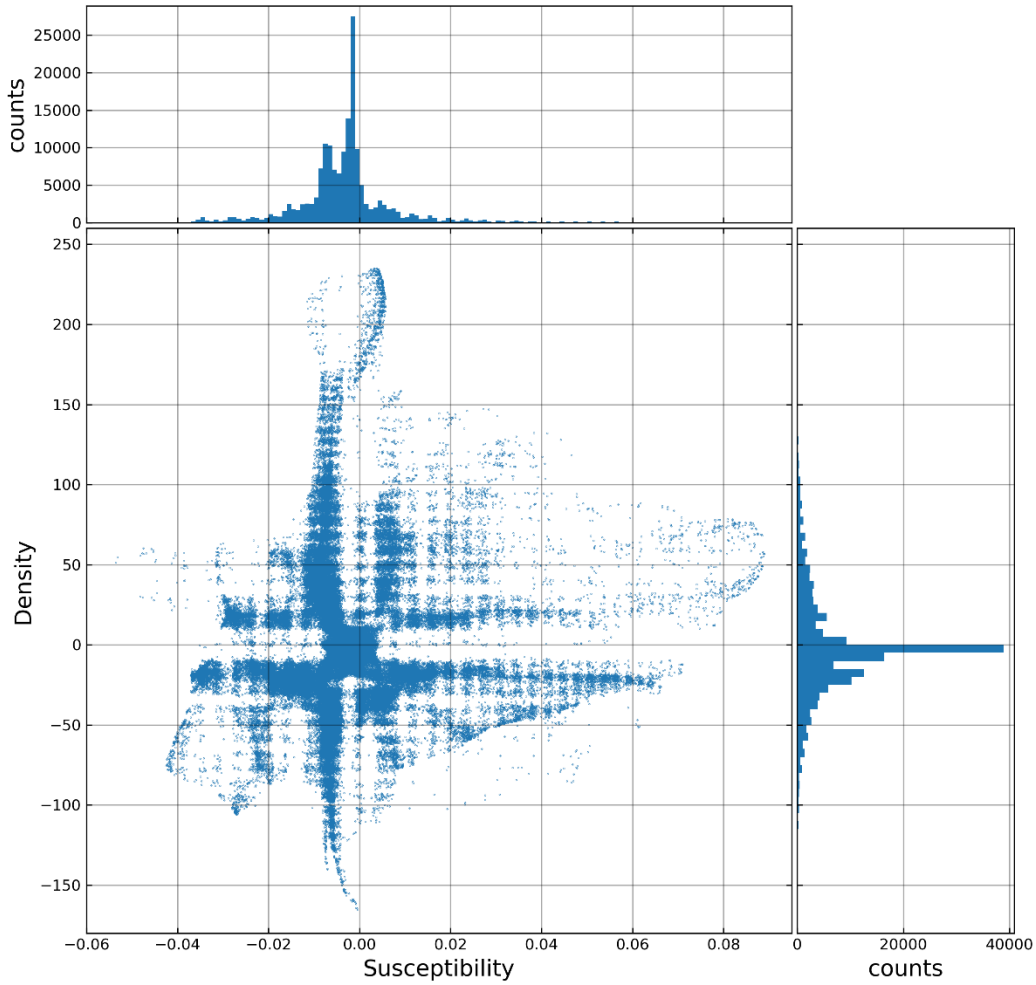

Figure 9: Inverted density and susceptibility cross plot and density and susceptibility histograms of the VI inversion model.

High relative density values above 100 kg/m^3 are located exclusively offshore while large negative values below -100 kg/m^3 are located as distinct cluster in the TAM and along the coast (Figure 10 a-b). High relative susceptibility values above 0.025 SI are located offshore and to a much larger extent at the western edge of the WSB at the inferred craton margin (Figure 10 a-b). Furthermore, strong negative relative susceptibility values below -0.03 SI are limited to the Craton margin (Figure 10 a-b).

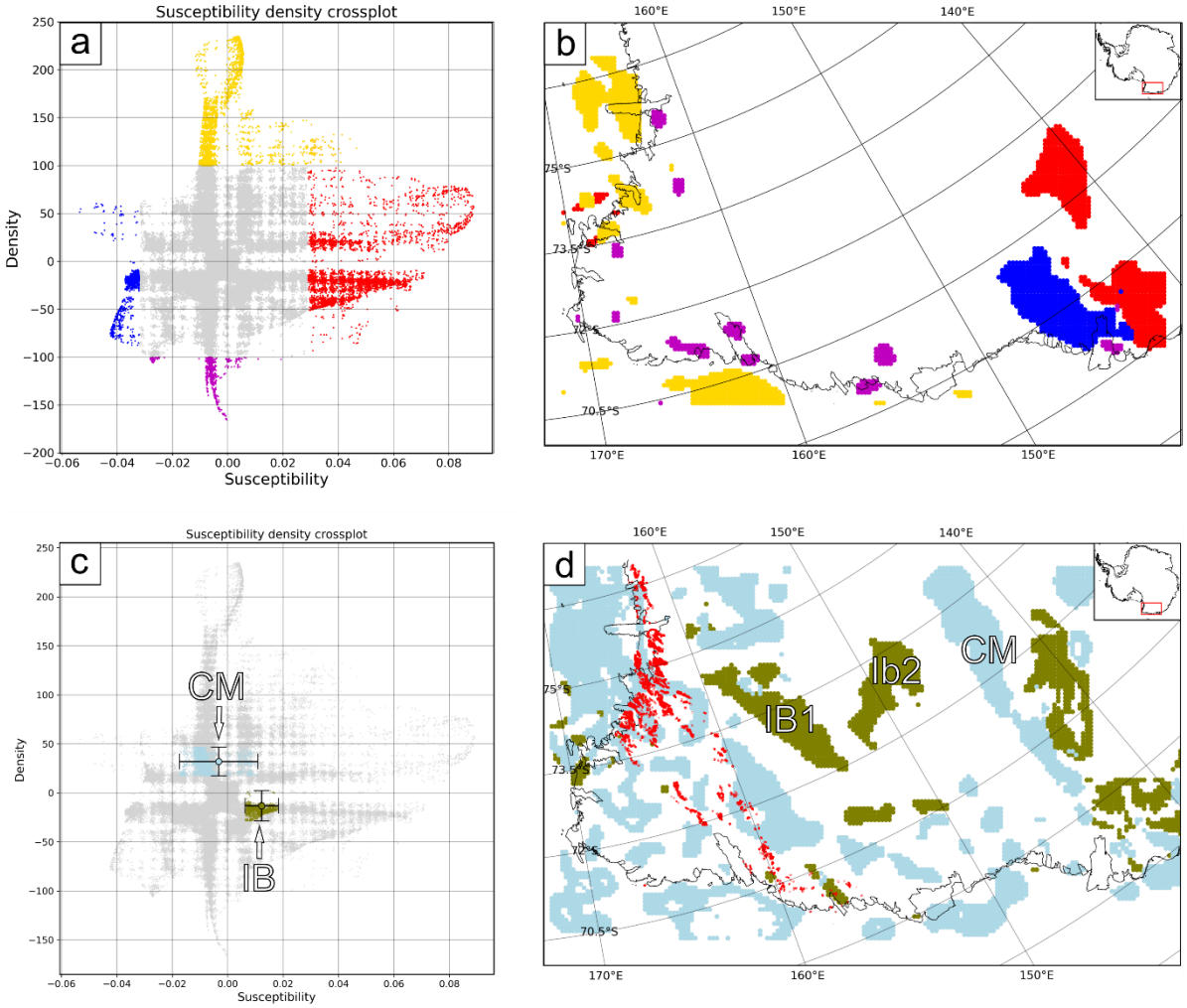

Figure 10: Density vs susceptibility cross-plots and province characterisation. a) Extreme susceptibility and density groupings. High inverted relative density values above 100 kg/m^3 (yellow dots), low relative inverted density values below – 100 kg/m^3 (purple dots), high relative inverted susceptibility values above 0.029 SI (red dots) and low relative inverted susceptibility values below -0.032 SI (blue dots) superimposed on density and susceptibility cross-plot of the entire inversion model. b) spatial distribution of extreme density and susceptibilities highlighted in a). c) density–susceptibility relationship of the interpreted intrusive bodies (olive green dots) and craton margin feature (light blue dots) superimposed on density and susceptibility cross-plot of the entire inversion model. d) location plot of density and susceptibility relationships within the standard deviation range of the extracted bodies in Figure 10 c. Granite Harbour Intrusive Complex (red) taken from GeoMAP [*Cox et al.*, 2023]. IB: intrusive body; CM: craton margin.

To constrain the geometry and properties of particular sub-surface source bodies we extracted the density and susceptibility values within the polygons p1 and p2 (polygon location shown in Figure 7 c-d) and subsequently used thresholding of the susceptibility or density values to recover the approximate geometry of sources associated with specific anomalies. The source for the prominent positive magnetic anomaly in the WSB region is extracted by windowing the joint inversion output in this area for relative susceptibility values larger than 0.003 SI. The volume of the extracted feature amounts to ~286 000 km^3. The source for the linear high gravity anomaly on the western flank of the

WSB was extracted by windowing the joint inversion output in this area for relative density values larger than 10 kg/m^3. The mean and standard deviation of the density and susceptibility relationship within those two extracted prominent features are superimposed on the density–susceptibility cross plot of the whole inversion model (Figure 10 c). Both features cluster around distinct areas in the cross plot and are easily distinguishable (Figure 10 c). The Central WSB source (IB1) has a mean relative density that is slightly negative and a mean relative susceptibility that is moderately positive, while the mean relative density is positive, and the mean relative susceptibility is negative for the feature along the craton margin (CM). The standard deviation for the susceptibility of the craton margin feature is significantly larger compared to the intrusion signal (Figure 10c). The standard deviation range of density and susceptibility for each body is subsequently used to filter the entire inversion model to find the location of rocks with matching density and susceptibility relationships across the study area (Figure 10 d). The location of rocks with matching susceptibility and density relationships reveals petrophysical similarities associated with the magnetic anomaly (F2 in Figure 3) adjacent to the central WSB magnetic anomaly (F1 in Figure 3), which potentially has the same origin (IB1, IB2 in Figure 10 d). The extent and volume of those 3D structures can be extracted from the model (Figure 11).

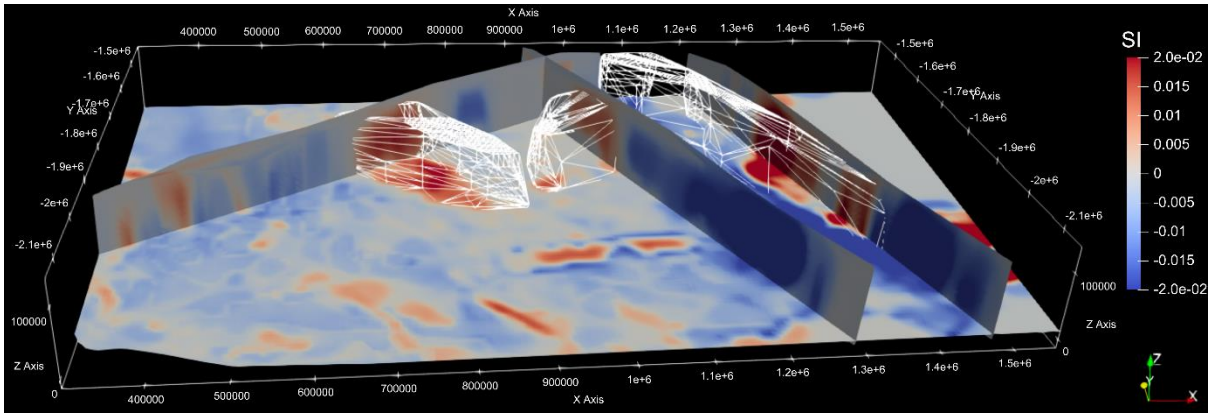

Figure 11: 3D intrusion and craton margin bodies (white wireframe) superimposed on slices through the 3D inverted susceptibility model. View looking grid north (approximately SSW geographically) along the axis of the WSB, with two interpreted intrusions in the centre and craton margin source body to the right.

5 Discussion

Shifting the relative density values to absolute values by adding the average crustal background density of 2670 kg/m^3 indicates that the density of the extracted feature in the centre of the WSB ranges from 2620 to 2690 km/m^3 combined with moderate susceptibility values. Based on its petrophysical properties and the large volume, we interpret this feature to be a granitic batholith intrusion. A previous geophysical interpretation that the origin of this feature is associated with thinned crust as a result of rifting [*Ferraccioli et al.*, 2001] can be ruled out since such a tectonic feature would have substantially higher densities than observed in the inversion model. This potentially granitic batholitic intrusion has the identical petrophysical signature in terms of density and susceptibility as the neighbouring body labelled IB2 in Figure (10d) which is associated with the magnetic anomaly labelled F2 in Figure (3 a, b). The density and susceptibility distribution along the AB profile (Figure 8 b-d) and the depth slices (Figure 7f) indicates that the sources for these anomalies (IB1 and IB2) are connected at depth. The total volume of the proposed batholith amounts to ~470 000 km^3, which is a significant addition to the volume of the upper crust at the time of emplacement. This block of intruded material very likely deviates from the surrounding rocks in terms of radiogenic heat production and thermal conductivity. Such broad crustal inhomogeneities or crustal blocks should be considered in future geothermal heat flow models of East Antarctica, even though the implementation is very challenging because the precise geochemical composition and the thermal petrophysical characteristics are unknown due to a lack of rock outcrops. The absence of the proposed granitic signature in the TAM is highly interesting, since granites from the Granite Harbour Igneous Complex are mapped and sampled by geological surveys in this area [*Cox et al.*, 2023]. This suggests that the petrological signature of the proposed batholithic intrusion body is fundamentally different from granites of the Granite Harbour Igneous Complex (Figure 10 d red dots) which was emplaced during the Ross Orogeny [*Estrada et al.*, 2016]. We speculate that the intrusion in the central WSB happened during the Pan African time (551 – 700 Ma) and is the source material of the Pan African-age zircons in the Priestley Formation [*Estrada et al.*, 2016]. Furthermore, a potential batholithic intrusion on such a scale will most certainly affect local crustal inhomogeneities and the local heat

411 flow budget even though the lack of direct geological samples and heat flow measurements makes it
412 challenging to quantify the extent. Even though the potential batholitic intrusion in the WSB is based
413 on geophysical interpretation and direct petrophysical and thermal property measurements are
414 lacking comparing the inferred batholith to direct measurements of potentially similar intrusive rocks
415 in the Weddell Sea [*Leat et al.*, 2018], the southern Przdz Bay [*Carson et al.*, 2014] and Cornwall
416 [*Beamish and Busby*, 2016] can inform which magnitude of heat flow elevation could be expected for
417 such a batholith, especially for East Antarctica were surface heat flow values are rarely predicted to
418 exceed ~60 mW/m^2 [*An et al.*, 2015; *Fox Maule et al.*, 2005; *Haeger et al.*, 2022; *Lösing and Ebbing*,
419 2021; *Lowe et al.*, 2023; *Martos et al.*, 2017; *Shen et al.*, 2020; *Stål et al.*, 2021]. A granitic batholithic
420 intrusion will increase the heat flow in this region significantly, especially when the granites are rich
421 in heat producing elements such as potassium (K), thorium (Th), and uranium (U). Evidence of high
422 heat producing granites exist in the Weddell Sea, which are responsible for significantly increasing the
423 local heat flow [*Leat et al.*, 2018]. Those granites, which intruded the West Antarctic crust are rich in
424 Th and U up to 60.7 and 28.6 ppm, respectively and lead to heat production of up to 9.06 µW/m^3 [*Leat*
425 *et al.*, 2018]. The local heat flow is predicted to reach 70-95 mW/m^2, which is 15-30 mW/m^2 higher
426 than the surrounding West Antarctic crust [*Leat et al.*, 2018] and is even higher compared to the colder
427 East Antarctic crust. Cambrian granites of southern Prydz Bay, East Antarctica, are reported to increase
428 local surface heat flow above 120 mW/m^2 [*Carson et al.*, 2014]. The Cornubian granite batholith
429 province in Cornwall, England, is one of the highest heat flow regions in the United Kingdom [*Beamish*
430 *and Busby*, 2016]. The Cornubian granite batholith stretches roughly 200 km through southwest
431 England and is comparable in size to the batholith in the central WSB. The heat flow within the
432 Cornubian granites is reported to be up to 138 mW/m^2 [*Beamish and Busby*, 2016]. This comparison
433 illustrates the magnitude of heat flow which is potentially underestimated in geophysical geothermal
434 heat flow models if the crustal domain is treated with global average values instead of accounting for
435 crustal heterogeneities.

436 The density and susceptibility relationship for the linear structure at the craton margin is more
437 ambiguous than the proposed batholith structures, due to the larger standard deviation in the
438 susceptibility values. Similar density and susceptibility relationships are present offshore, and onshore
439 along the cost and in the TAM, but these areas may be lithologically distinct from the craton margin
440 structure. We propose that the linear craton margin feature can be interpreted as the remnant
441 signature of a former magmatic rifted continental margin where thick sequences of seaward dipping
442 basalt horizons are often combined with mafic underplating. Both features require densities above
443 2700 kg/m^3, in line with the inversion result. Additionally, both features host the potential of
444 significant remanent magnetisation, as indicated by negative relative susceptibility. An alternative
445 model for the positive gravity anomaly associated with the margin of the East Antarctic craton inboard
446 from the WSB proposed by [*Studinger et al.*, 2004] is that of a section of up-thrust crustal material
447 loading the craton margin. Our inversion does not show the strongly asymmetric pattern of densities
448 expected for a flexural loaded margin, but we can-not rule out some amount of compressional re-
449 working of the former rifted margin during the Ross Orogeny.

450 Our inversion results and the density – susceptibility relationship indicate that a large-scale batholitic
451 intrusion is present in the WSB. We speculate that this was emplaced during the Pan African time, and
452 is not connected to the Granite Harbour Igneous Complex, which was emplaced slightly later during
453 the Ross Orogeny [*Estrada et al.*, 2016]. Furthermore, the highly variable susceptibility values in the
454 west towards the craton margin combined with the high-density bodies could indicate thick seaward
455 dipping basalt horizons coupled with mafic magmatic underplating, which can both have high
456 susceptibility and potentially hold strong remanent magnetisation, giving rise to the recovered
457 negative relative susceptibility values. Based on those findings we propose a four-step tectonic
458 evolution (Figure 12), which includes the initial development of a rifted continental margin with
459 seaward dipping basalt horizons and mafic underplating, followed by passive margin development and
460 two distinct subsequent intrusion events to emplace the proposed “Central Batholith” and the Granite
461 Harbour Igneous Complex. We speculate that these were resulted from subduction-related magmatic

462 arc formation. The age of the initial rifting event is unknown, but evidence of rifting and passive margin
463 development in the Central Transantarctic Mountains suggests that this may have occurred around
464 670 Ma [*Goodge*, 2020; *Goodge et al.*, 2002]. We propose that the Central Batholith was emplaced
465 after development of a subduction system against the former passive margin. This batholith may be
466 the source for the ~650 Ma zircon ages found in sedimentary rocks in the Priestly formation [*Estrada*
467 *et al.*, 2016]. Emplacement of the Central Batholith was followed by the Ross age (550 - 450 Ma)
468 emplacement of the Granite Harbour Igneous Complex.

469 In summary, we propose a four-stage geodynamic evolution model for this region. Stage 1: ~670 Ma:
470 Continental breakup and a developing magmatic rifted margin with seaward dipping basalt horizons
471 and mafic underplating. Stage 2: ~660 Ma continued ocean spreading and sediment deposition on the
472 shelf of the passive margin. Stage 3: ~650 Ma Arc development as a result of subduction against
473 continental margin. Large scale emplacement of Batholith intrusion, potential re-working and back
474 thrusting of mafic components onto the craton. Stage 4: ~500 Subduction zone retreat associated with
475 secondary arc development and emplacement of intrusive rocks of the Granite Harbour Igneous
476 Complex in bound to the TAM.

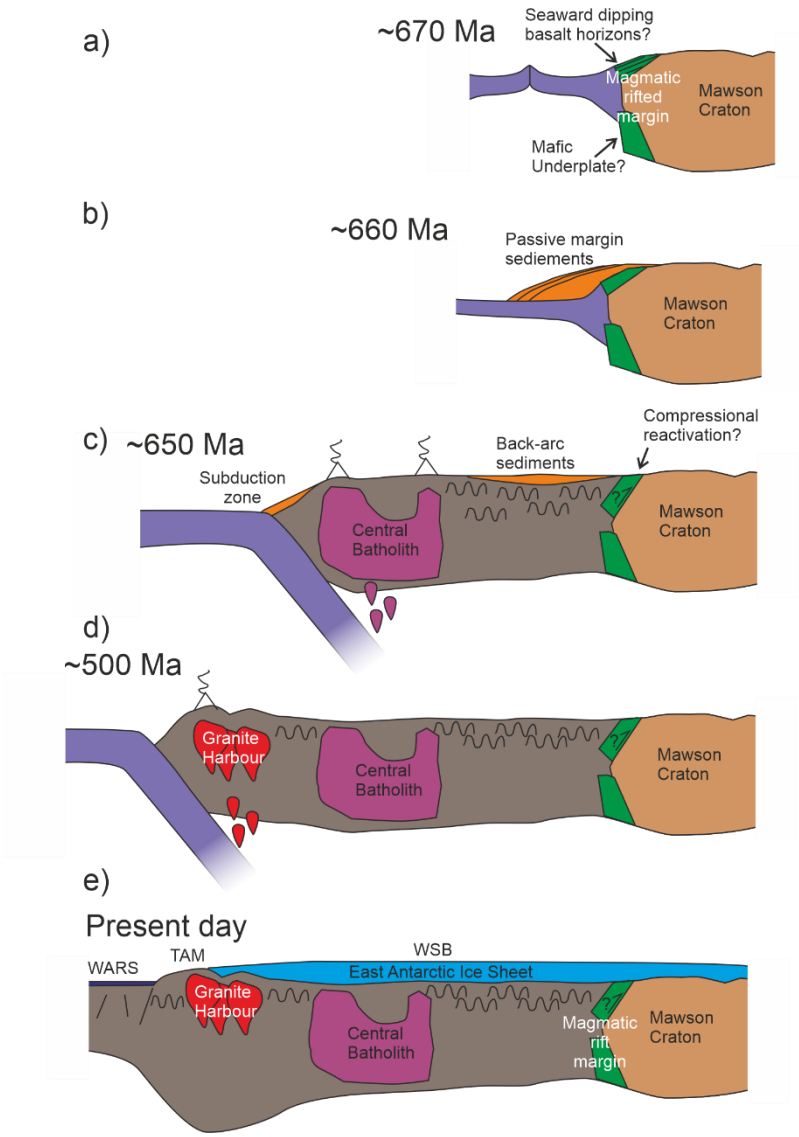

Figure 12: Tectonic evolution sketch: a) Rifting of Rodinia supercontinent and development of magmatic margin. b) Passive margin development and sediment deposition. c) Subduction zone development, emplacement of Central Batholith, re-working of passive margin and potentially deposition of back-arc sediments. d) Subduction zone migrates further out-board and Granite Harbour intrusive suite is emplaced. e) Present day geological section.

6 Conclusion and Future Work

We present a density and susceptibility distribution model for the Wilkes Subglacial Basin and the Transantarctic Mountains using joint inversion of gravity and magnetic data based on variation of information coupling. This model provides insight into the heterogeneity of the 3D crustal structure in The WSB and TAM region and allows quantification of the volume of crustal provinces which should be considered in future lithospheric scale thermal studies. The inversion model images a large low density and moderate susceptibility body in the central WSB, which we interpreted as most likely to

be an intrusive granite batholith based on the inverted petrophysical properties. A failed rift scenario for the origin of this body can be ruled out based on the inverted petrophysical relationship. Furthermore, the density and susceptibility relationship and cross-section of the inversion model indicates that this structure is connected to the adjacent low density moderate susceptibility body, which potentially has the same origin but nearly perpendicular orientation. If so the volume of the total granitic intrusive body increases to ~470 000 km^3, which is a considerable amount of addition volume of the upper crust at the time of emplacement phase that has the potential to have an enduring effect on the local heat flow due to radiogenic decay of heat producing elements. Despite the lack of direct heat production and heat flow measurements, correlation to well-studied granite intrusion provinces in the Weddell Sea [*Leat et al.*, 2018], southern Prydz Bay [*Carson et al.*, 2014], and Cornwall [*Beamish and Busby*, 2016] emphasise the influence local crustal structures such as intrusive bodies can have on the local heat flow budget.

Examining the density and susceptibility relationship we found that the batholith intrusion has a different petrophysical signature to the Granite Harbour Igneous Complex. Furthermore, the edge of the craton is identified by the inversion in the form of a positive linear gravity anomaly west of the WSB. Based on our findings the tectonic evolution of the WSB requires two distinct intrusion events emplacing the batholith and subsequently emplacing the Granite Harbour Igneous Complex. The inverted crustal model supports the idea of a passive continental margin with thick seaward dipping basalt horizons and mafic underplating. However, the alternative idea of up-thrusted crustal material at the craton edge cannot be ruled out based on the geophysical inversion model. Combined scenarios between these endmember models are also possible.

This study highlights the crustal heterogeneities on a regional scale in East Antarctica and gives evidence that treating the crustal domain with a set of constant global average values in geophysical geothermal heat flow models is a simplification that might underestimate the geothermal heat flow beneath the ice sheets. Despite the many challenges, next generations of geophysical heat flow

models are required to consider crustal heterogeneities to increase the understanding of the contribution from the solid earth to the cryosphere and ultimately the stability of the ice sheet. Therefore, further geophysical, and geological research on the Antarctic subglacial geology is necessary to understand the thermal state of the most remote continent on Earth.

Acknowledgements

Funding for this research was provided by NERC through a SENSE CDT studentship (NE/T00939X/1). ML acknowledges additional funding through the Gray-Milne Travel Bursary provided by the British Geophysical Association and the Small IT grant awarded by the School of GeoSciences, The University of Edinburgh. The authors thank the developers of open scientific software products and colormap products which were utilized in this study: JIF3D is available under a GNU General Public License (v3) via subversion at https://svn.code.sf.net/p/jif3d/jif3dsvn/trunk/jif3D; NumPy [*Harris et al.*, 2020], Matplotlib [*Hunter*, 2007]; Pandas [*McKinney*, 2010]; Geopandas [*Jordahl et al.*, 2020]; Cmrameri [*Crameri*, 2023]; Cartopy [*Elson et al.*, 2022]; Shapley [*Gillies et al.*, 2022]; SciPy [*Virtanen et al.*, 2020]; PyKrige [*Murphy et al.*, 2022] and Jupyter notebook [*Kluyver et al.*, 2016] as well as the developer of the commercial software Geosoft, especially the plug-in "Compudrape" and their publisher Seequent.

Open Research

Python code in form of a Jupyter notebooks to reproduce the inversion and plot the inversion results are temporarily available at GitHub (https://github.com/MaximilianLowe/VI_inversion_WSB_TAM_JGRse). The GitHub repository will be transferred to zenodo after the manuscript is accepted.

Inversion models will be available and archived at the British Antarctic Survey Polar data centre as netCDF files. The data is transferred but not jet published (usually takes a few weeks). In the meantime, for the review process the netCDF files can be access through following link: https://www.dropbox.com/scl/fo/uqlsm50cf6ykkcje1ke41/h?rlkey=8y90rjwlwefmnlj4l1qdwxoxu&dl=0

BedMachine Antarctica version 3 [*Morlighem et al.*, 2020] is freely available at https://nsidc.org/data/nsidc-0756/versions/3

ADMAP-2 magnetic data [*Golynsky et al.*, 2018] is freely available at https://doi.pangaea.de/10.1594/PANGAEA.892724

AntGG [*Scheinert et al.*, 2016] is available at: https://doi.pangaea.de/10.1594/PANGAEA.892724

Curie point depths [*Lowe et al.*, 2022] are available at: https://ramadda.data.bas.ac.uk/repository/entry/show?entryid=b8dcbaa9-3ac0-42bd-95a5-6b5961cbcb7e

Moho depth [*Pappa et al.*, 2019a] are available from: https://agupubs.onlinelibrary.wiley.com/action/downloadSupplement?doi=10.1029%2F2018GC008111&file=GGGE_21848_DataSetsS1-S6.zip.

References

An, M., D. A. Wiens, Y. Zhao, M. Feng, A. Nyblade, M. Kanao, Y. Li, A. Maggi, and J.-J. Lévêque (2015), Temperature, lithosphere-asthenosphere boundary, and heat flux beneath the Antarctic Plate inferred from seismic velocities, *Journal of Geophysical Research: Solid Earth*, *120*(12), 8720-8742.

Artemieva, I. M., and W. D. Mooney (2001), Thermal thickness and evolution of Precambrian lithosphere: A global study, *Journal of Geophysical Research: Solid Earth*, *106*(B8), 16387-16414.

Avdeev, D., and A. Avdeeva (2009), 3D magnetotelluric inversion using a limited-memory quasi-Newton optimization, *GEOPHYSICS*, *74*(3), F45-F57.

Beamish, D., and J. Busby (2016), The Cornubian geothermal province: heat production and flow in SW England: estimates from boreholes and airborne gamma-ray measurements, *Geothermal Energy*, *4*(1), 4.

Bosch, M., R. Meza, R. Jiménez, and A. Hönig (2006), Joint gravity and magnetic inversion in 3D using Monte Carlo methods, *GEOPHYSICS*, *71*(4), G153-G156.

Burton-Johnson, A., R. Dziadek, and C. Martin (2020), Review article: Geothermal heat flow in Antarctica: current and future directions, *The Cryosphere*, *14*(11), 3843-3873.

Carson, C. J., S. McLaren, J. L. Roberts, S. D. Boger, and D. D. Blankenship (2014), Hot rocks in a cold place: high sub-glacial heat flow in East Antarctica, *Journal of the Geological Society*, *171*(1), 9-12.

Cox, S. C., et al. (2023), The GeoMAP (v.2022-08) continent-wide detailed geological dataset of Antarctica, edited, PANGAEA.

Crameri, F. (2023), Scientific colour maps, edited, Zenodo.

DeConto, R. M., and D. Pollard (2016), Contribution of Antarctica to past and future sea-level rise, *Nature*, *531*(7596), 591-597.

Drewry, D., J. (1976), Sedimentary basins of the east antarctic craton from geophysical evidence, *Tectonophysics*, *36*(1), 301-314.

Elson, P., et al. (2022), SciTools/cartopy: v0.21.1, edited, Zenodo.

Estrada, S., A. Läufer, K. Eckelmann, M. Hofmann, A. Gärtner, and U. Linnemann (2016), Continuous Neoproterozoic to Ordovician sedimentation at the East Gondwana margin — Implications from detrital zircons of the Ross Orogen in northern Victoria Land, Antarctica, *Gondwana Research*, *37*, 426-448.

Ferraccioli, F., and E. Bozzo (2003), Cenozoic strike-slip faulting from the eastern margin of the Wilkes Subglacial Basin to the western margin of the Ross Sea Rift: an aeromagnetic connection, *Geological Society, London, Special Publications*, *210*(1), 109-133.

Ferraccioli, F., E. Armadillo, T. A. Jordan, E. Bozzo, and H. Corr (2009a), Aeromagnetic exploration over the East Antarctic Ice Sheet: A new view of the Wilkes Subglacial Basin, *Tectonophysics*, *478*(1), 62-77.

Ferraccioli, F., E. Armadillo, A. Zunino, E. Bozzo, S. Rocchi, and P. Armienti (2009b), Magmatic and tectonic patterns over the Northern Victoria Land sector of the Transantarctic Mountains from new aeromagnetic imaging, *Tectonophysics*, *478*(1), 43-61.

Ferraccioli, F., F. Coren, E. Bozzo, C. Zanolla, S. Gandolfi, I. Tabacco, and M. Frezzotti (2001), Rifted(?) crust at the East Antarctic Craton margin: gravity and magnetic interpretation along a traverse across the Wilkes Subglacial Basin region, *Earth and Planetary Science Letters*, *192*(3), 407-421.

Ferré, E. C., S. A. Friedman, F. Martín-Hernández, J. M. Feinberg, J. L. Till, D. A. Ionov, and J. A. Conder (2014), Eight good reasons why the uppermost mantle could be magnetic, *Tectonophysics*, *624-625*, 3-14.

Fox Maule, C., M. E. Purucker, N. Olsen, and K. Mosegaard (2005), Heat Flux Anomalies in Antarctica Revealed by Satellite Magnetic Data, *Science*, *309*(5733), 464-467.

Fregoso, E., and L. A. Gallardo (2009), Cross-gradients joint 3D inversion with applications to gravity and magnetic data, *GEOPHYSICS*, *74*(4), L31-L42.
Frey, M., and J. Ebbing (2020), The deep geothermal potential of the radiogenic Løvstakken Granite in western Norway, *Norwegian Journal of Geology/Norsk Geologisk Forening*, *100(1)*.
Gallardo-Delgado, L. A., M. A. Pérez-Flores, and E. Gómez-Treviño (2003), A versatile algorithm for joint 3D inversion of gravity and magnetic data, *GEOPHYSICS*, *68*(3), 949-959.
Gillies, S., C. van der Wel, J. Van den Bossche, M. W. Taves, J. Arnott, B. C. Ward, and a. others (2022), Shapely, edited, Zenodo.
Golynsky, A. V., et al. (2018), New Magnetic Anomaly Map of the Antarctic, *Geophysical Research Letters*, *45*(13), 6437-6449.
Goodge, J. W. (2020), Geological and tectonic evolution of the Transantarctic Mountains, from ancient craton to recent enigma, *Gondwana Research*, *80*, 50-122.
Goodge, J. W., and C. A. Finn (2010), Glimpses of East Antarctica: Aeromagnetic and satellite magnetic view from the central Transantarctic Mountains of East Antarctica, *Journal of Geophysical Research: Solid Earth*, *115*(B9).
Goodge, J. W., P. Myrow, I. S. Williams, and S. A. Bowring (2002), Age and Provenance of the Beardmore Group, Antarctica: Constraints on Rodinia Supercontinent Breakup, *The Journal of Geology*, *110*(4), 393-406.
Guillen, A., and V. Menichetti (1984), Gravity and magnetic inversion with minimization of a specific functional, *GEOPHYSICS*, *49*(8), 1354-1360.
Haber, E., and M. Holtzman Gazit (2013), Model Fusion and Joint Inversion, *Surveys in Geophysics*, *34*(5), 675-695.
Haeger, C., A. G. Petrunin, and M. K. Kaban (2022), Geothermal Heat Flow and Thermal Structure of the Antarctic Lithosphere, *Geochemistry, Geophysics, Geosystems*, *23*(10), e2022GC010501.
Harris, C. R., et al. (2020), Array programming with NumPy, *Nature*, *585*(7825), 357-362.
Hasterok, D., and D. S. Chapman (2011), Heat production and geotherms for the continental lithosphere, *Earth and Planetary Science Letters*, *307*(1), 59-70.
Hunter, J. (2007), Matplotlib: A 2D Graphics Environment, *Computing in Science & Engineering*, *9*(3), 90-95.
Jordahl, K., et al. (2020), geopandas/geopandas: v0.8.1, edited, Zenodo.
Jordan, T. A., F. Ferraccioli, E. Armadillo, and E. Bozzo (2013), Crustal architecture of the Wilkes Subglacial Basin in East Antarctica, as revealed from airborne gravity data, *Tectonophysics*, *585*, 196-206.
Kluyver, T., et al. (2016), Jupyter Notebooks—a publishing format for reproducible computational workflows, *Positioning and Power in Academic Publishing: Players, Agents and Agendas, IOS Press (2016)*, 87-90.
Leat, P. T., T. A. Jordan, M. J. Flowerdew, T. R. Riley, F. Ferraccioli, and M. J. Whitehouse (2018), Jurassic high heat production granites associated with the Weddell Sea rift system, Antarctica, *Tectonophysics*, *722*, 249-264.
Lösing, M., and J. Ebbing (2021), Predicting Geothermal Heat Flow in Antarctica With a Machine Learning Approach, *Journal of Geophysical Research: Solid Earth*, *126*(6), e2020JB021499.
Lösing, M., M. Moorkamp, and J. Ebbing (2023), Joint Inversion Based on Variation of Information - A Crustal Model of Wilkes Land, East Antarctica, *Geophysical Journal International*.
Lowe, M., B. Mather, C. Green, T. A. Jordan, J. Ebbing, and R. Larter (2022), Curie depth points and Geothermal heat flow estimates from spectral analysis of magnetic data in the Transantarctic Mountains and Wilkes Subglacial Basin region. (Version 1.0) [Data set]. edited, NERC EDS UK Polar Data Centre.
Lowe, M., B. Mather, C. Green, T. A. Jordan, J. Ebbing, and R. Larter (2023), Anomalously High Heat Flow Regions Beneath the Transantarctic Mountains and Wilkes Subglacial Basin in East Antarctica Inferred From Curie Depth, *Journal of Geophysical Research: Solid Earth*, *128*(1), e2022JB025423.

Mandolesi, E., and A. G. Jones (2014), Magnetotelluric inversion based on mutual information, *Geophysical Journal International*, *199*(1), 242-252.
Martos, Y. M., M. Catalán, T. A. Jordan, A. Golynsky, D. Golynsky, G. Eagles, and D. G. Vaughan (2017), Heat Flux Distribution of Antarctica Unveiled, *Geophysical Research Letters*, *44*(22), 11,417-411,426.
McKinney, W. (2010), Data structures for statistical computing in python, *Proceedings of the 9th Python in Science Conference*, *445*(1), 51-56.
Moorkamp, M. (2021), Joint inversion of gravity and magnetotelluric data from the Ernest-Henry IOCG deposit with a variation of information constraint, in *First International Meeting for Applied Geoscience & Energy Expanded Abstracts*, edited, pp. 1711-1715.
Moorkamp, M. (2022), Deciphering the State of the Lower Crust and Upper Mantle With Multi-Physics Inversion, *Geophysical Research Letters*, *49*(9), e2021GL096336.
Moorkamp, M., B. Heincke, M. Jegen, A. W. Roberts, and R. W. Hobbs (2011), A framework for 3-D joint inversion of MT, gravity and seismic refraction data, *Geophysical Journal International*, *184*(1), 477-493.
Morelli, A., and S. Danesi (2004), Seismological imaging of the Antarctic continental lithosphere: a review, *Global and Planetary Change*, *42*(1), 155-165.
Morlighem, M., et al. (2020), Deep glacial troughs and stabilizing ridges unveiled beneath the margins of the Antarctic ice sheet, *Nature Geoscience*, *13*(2), 132-137.
Murphy, B., R. Yurchak, and S. Müller (2022), GeoStat-Framework/PyKrige: v1.7.0, *Zenodo*.
Pappa, F., J. Ebbing, and F. Ferraccioli (2019a), Moho Depths of Antarctica: Comparison of Seismic, Gravity, and Isostatic Results, *Geochemistry, Geophysics, Geosystems*, *20*(3), 1629-1645.
Pappa, F., J. Ebbing, F. Ferraccioli, and W. van der Wal (2019b), Modeling Satellite Gravity Gradient Data to Derive Density, Temperature, and Viscosity Structure of the Antarctic Lithosphere, *Journal of Geophysical Research: Solid Earth*, *124*(11), 12053-12076.
Paxman, G. J. G., S. S. R. Jamieson, F. Ferraccioli, M. J. Bentley, N. Ross, E. Armadillo, E. G. W. Gasson, G. Leitchenkov, and R. M. DeConto (2018), Bedrock Erosion Surfaces Record Former East Antarctic Ice Sheet Extent, *Geophysical Research Letters*, *45*(9), 4114-4123.
Paxman, G. J. G., S. S. R. Jamieson, F. Ferraccioli, M. J. Bentley, N. Ross, A. B. Watts, G. Leitchenkov, E. Armadillo, and D. A. Young (2019), The Role of Lithospheric Flexure in the Landscape Evolution of the Wilkes Subglacial Basin and Transantarctic Mountains, East Antarctica, *Journal of Geophysical Research: Earth Surface*, *124*(3), 812-829.
Pollard, D., R. M. DeConto, and R. B. Alley (2015), Potential Antarctic Ice Sheet retreat driven by hydrofracturing and ice cliff failure, *Earth and Planetary Science Letters*, *412*, 112-121.
Reading, A. M., T. Stål, J. A. Halpin, M. Lösing, J. Ebbing, W. Shen, F. S. McCormack, C. S. Siddoway, and D. Hasterok (2022), Antarctic geothermal heat flow and its implications for tectonics and ice sheets, *Nature Reviews Earth & Environment*, *3*(12), 814-831.
Reitmayr, G., W. Korth, G. Caneva, and F. Ferraccioli (2003), Gravity Survey at the Oates Coast Area, East Antarctica, during the Joint German-Italian Expedition 1999/2000, *TERRA ANTARTICA*, *10*, 97-104.
Robinson, E. S., and J. F. Splettstoesser (1986), Structure of the Transantarctic Mountains Determined From Geophysical Surveys, in *Geology of the Central Transantarctic Mountains*, edited, pp. 119-162.
Scheinert, M., et al. (2016), New Antarctic gravity anomaly grid for enhanced geodetic and geophysical studies in Antarctica, *Geophysical Research Letters*, *43*(2), 600-610.
Schoof, C. (2007), Ice sheet grounding line dynamics: Steady states, stability, and hysteresis, *Journal of Geophysical Research: Earth Surface*, *112*(F3).
Shamsipour, P., D. Marcotte, and M. Chouteau (2012), 3D stochastic joint inversion of gravity and magnetic data, *Journal of Applied Geophysics*, *79*, 27-37.
Shen, W., D. A. Wiens, A. J. Lloyd, and A. A. Nyblade (2020), A Geothermal Heat Flux Map of Antarctica Empirically Constrained by Seismic Structure, *Geophysical Research Letters*, *47*(14), e2020GL086955.
Stål, T., A. M. Reading, J. A. Halpin, and J. M. Whittaker (2021), Antarctic Geothermal Heat Flow Model: Aq1, *Geochemistry, Geophysics, Geosystems*, *22*(2), e2020GC009428.

696 Steed, R. N. (1983), Structural interpretations of Wilkes Land, Antarctica, *Antarctic earth science. International symposium*, *4*.
698 Stern, T. A., and U. ten Brink, S. (1989), Flexural uplift of the Transantarctic Mountains, *Journal of Geophysical Research: Solid Earth*, *94*(B8), 10315-10330.
700 Stokes, C. R., et al. (2022), Response of the East Antarctic Ice Sheet to past and future climate change, *Nature*, *608*(7922), 275-286.
702 Studinger, M., R. E. Bell, W. R. Buck, G. D. Karner, and D. D. Blankenship (2004), Sub-ice geology inland of the Transantarctic Mountains in light of new aerogeophysical data, *Earth and Planetary Science Letters*, *220*(3), 391-408.
705 ten Brink, U., S., and T. Stern (1992), Rift flank uplifts and Hinterland Basins: Comparison of the Transantarctic Mountains with the Great Escarpment of southern Africa, *Journal of Geophysical Research: Solid Earth*, *97*(B1), 569-585.
708 ten Brink, U., S., R. I. Hackney, S. Bannister, T. A. Stern, and Y. Makovsky (1997), Uplift of the Transantarctic Mountains and the bedrock beneath the East Antarctic ice sheet, *Journal of Geophysical Research: Solid Earth*, *102*(B12), 27603-27621.
711 Virtanen, P., et al. (2020), SciPy 1.0: fundamental algorithms for scientific computing in Python, *Nature Methods*, *17*(3), 261-272.
713 Zanutta, A., M. Negusini, L. Vittuari, L. Martelli, P. Cianfarra, F. Salvini, F. Mancini, P. Sterzai, M. Dubbini, and A. Capra (2018), New Geodetic and Gravimetric Maps to Infer Geodynamics of Antarctica with Insights on Victoria Land, *Remote Sensing*, *10*(10), 1608.

716